Ultrafine Graphene Nanomesh with Large On/Off Ratio for High-Performance Flexible Biosensors

Yanbing Yang, Xiangdong Yang, Xuming Zou, Shiting Wu, Da Wan, Anyuan Cao, Lei Liao, Quan Yuan,* and Xiangfeng Duan**

Graphene is an attractive material for flexible electronics and biosensors, yet its zero bandgap nature has limited the on/off ratio of field-effect transistors (FETs) and the sensitivity of biosensors based on graphene. Graphene nanomesh (GNM), a continuous 2D graphene nanostructure with a high density of holes punched in the basal plane, has been created to introduce lateral confinement and enable improved on/off ratio. However, the GNMs produced to date typically have a relatively large dimension (constriction neck width >5 nm) and low on/off ratio (≈100) limited by the resolution of the lithography process used. Here, the exploration of a directly grown mesoporous silica template is reported for the preparation of ultrafine GNMs with considerably narrower neck width (<3 nm) and strong quantum confinement to enable flexible FETs with greatly improved on/off ratio (up to 1000). With excellent electronic properties and high surface area for the functionalization of specific receptors, it is further shown that the GNM FETs can be readily used to construct highly sensitive biosensors for selective detection of human epidermal growth factor receptor 2, which is further demonstrated for real-time detection of breast cancer cells overexpressed with receptor 2 down to single-cell level. The studies provide a simple and scalable method to GNMs with potential applications for flexible nanoelectronics and biosensors.

1. Introduction

Flexible electronics that can accommodate dramatic shape deformations while maintaining their intrinsic performance are of increasing interest for a new generation of wearable devices.[1–3] As a type of flexible electronics, implantable flexible biosensors that provide continuous and real-time measurement of biomarkers have gained much recent attention.[4–8] Because of their extraordinary electronic characteristics, particularly the ultrahigh carrier mobility and highly tunable electronic properties,[9–13] graphene-based materials hold great promise for constructing highly sensitive biosensors. By incorporating functional groups with specific chemical or biological recognition ability, graphene-based biosensors can be utilized to detect multiple biomolecules, such as DNA,[14] protein,[15–17] glucose,[18] dopamine,[19] etc. For example, Knoll and co-workers demonstrated an olfactory biosensor based on a reduced graphene oxide (rGO) field-effect transistor (FET) functionalized by the odorant-binding protein 14 for the in situ and real-time monitoring of a broad spectrum of odorants in aqueous solutions.[20] Haghiri-Gosnet and co-workers recently reported an electrochemical biosensor based on graphene nanomesh with 260 nm wide nanoholes for the ultrasensitive detection of DNA.[21] Furthermore, with a single-atom-thick 2D honeycomb lattice of covalently bonded carbon atoms, graphene exhibits exceptional mechanical strength and flexibility and is ideally for flexible biosensor applications.[22–25] Hong and co-workers prepared a flexible paraoxon electrochemical biosensor using self-assembled rGO and nafion hybrids.[26] Jang and co-workers fabricated a liquid-ion gated FET flexible fluidic HIV immunosensor based on arranged graphene micropattern nanobiohybrids.[27] However, the zero bandgap and semimetallic nature of graphene have limited the on/off ratio of graphene-based transistors and the sensitivity of such transistor-based sensors, making them ill-suited for practical applications in monitoring biomarkers that are typically in the nanomolar regime.

The creation of graphene nanostructures with lateral quantum confinement has been broadly explored to introduce finite bandgap and thus improve the on/off ratio. Thus far, methods including lithography,[28–31] chemistry,[32,33] surface modification,[34,35] and unzipping carbon nanotubes[36] have

Y. B. Yang, X. D. Yang, Prof. Q. Yuan
Key Laboratory of Analytical Chemistry for Biology and Medicine (Ministry of Education)
College of Chemistry and Molecular Sciences
Wuhan University
Wuhan 430072, China
E-mail: yuanquan@whu.edu.cn
Prof. X. F. Duan
Department of Chemistry and Biochemistry
University of California
Los Angeles, CA 90095, USA
E-mail: xduan@chem.ucla.edu
Dr. X. M. Zou, D. Wan, Prof. L. Liao
Department of Physics and Key Laboratory of Artificial Micro- and Nano-structures of Ministry of Education
Wuhan University
Wuhan 430072, China
E-mail: liaolei@whu.edu.cn
S. T. Wu, Prof. A. Y. Cao
Department of Materials Science and Engineering
College of Engineering
Peking University
Beijing 100871, China

DOI: 10.1002/adfm.201604096

been developed to open the bandgap in graphene.[37] However, since it requires complicated and precise techniques to control the sample preparation conditions, those processes suffered from low throughput and high production cost. Additionally, the low surface area of the as-grown graphene limits the effective interaction between receptors and ligands. To date, the development of a simple, low cost, and scalable production technique to large area graphene with a finite bandgap and large surface area remains a great challenge.

Graphene nanomesh (GNM), a continuous 2D graphene nanostructure with a high density of holes punched in the basal plane, has been created to introduce lateral confinement and enable improved on/off ratio.[38–42] However, the GNMs produced to date typically have a relatively large dimension (constriction neck width >5 nm) and low on/off ratio (≈100) limited by the resolution of the lithography processes used. Here, we report the exploration of a directly grown mesoporous silica (meso-SiO_2) template for the preparation of ultrafine GNMs with considerably narrower neck width (<3 nm) and strong quantum confinement to enable flexible FETs with greatly improved on/off ratio (up to 1000). With excellent electronic properties and high surface area for the functionalization of specific receptors, we demonstrate, for the first time, that GNM-FETs can be used to construct highly sensitive biosensors for selective detection of key biomarkers and cells for breast cancer. To our best knowledge, this is the first demonstration of the large area uniform GNMs with ultranarrow neck width (<3 nm), and the first application of GNMs for high-performance flexible biosensors. It is anticipated that our demonstration of ultrafine GNMs not only represents a method for opening bandgap in graphene but also for fabricating high-performance flexible biosensors in cost-effective and time efficient ways.

2. Results and Discussion

The fabrication route toward ultrafine GNMs is schematically illustrated in **Figure 1**a. First, large area graphene grown by chemical vapor deposition (CVD) (see the Experimental Section in the Supporting Information) was transferred onto a mechanically flexible polyethylene terephthalate (PET) substrate, which served as the starting material. A uniform and continuous meso-SiO_2 film with perpendicular mesoporous channels was next coated onto the graphene surface by a simple Stöber-solution growth method, which involves a micelle assembly process and simultaneous hydrolysis and condensation of precursors.[43] O_2 plasma etching was then used to punch holes into the graphene layer and a subsequent hydrofluoric acid dip was used to remove the meso-SiO_2 layer and produce GNM with uniformly arranged pores. The optical image in Figure 1a shows that the resulting GNM retains its original integrity and transparency.

To unambiguously determine the GNM structure, we carried out extensive scanning electron microscopy and transmission electron microscopy (TEM) studies. The single-layer GNM shows a large and smooth surface (Figure 1b; Figure S1, Supporting Information) without discontinuous domains, demonstrating that our approach is effective for the fabrication of a large area uniform GNM. Additionally, the typical periodically arranged pores are clearly seen (Figure 1b), which is consistent with the structure of meso-SiO_2 film (Figure S3, Supporting Information). Scanning tunneling microscopy (STM) characterization of the pristine graphene clearly shows the single-layer structure with honeycomb lattice of carbon atoms arranged in six-membered rings (Figure 1c). However, the STM topographic image of the GNM exhibits two distinct contrast

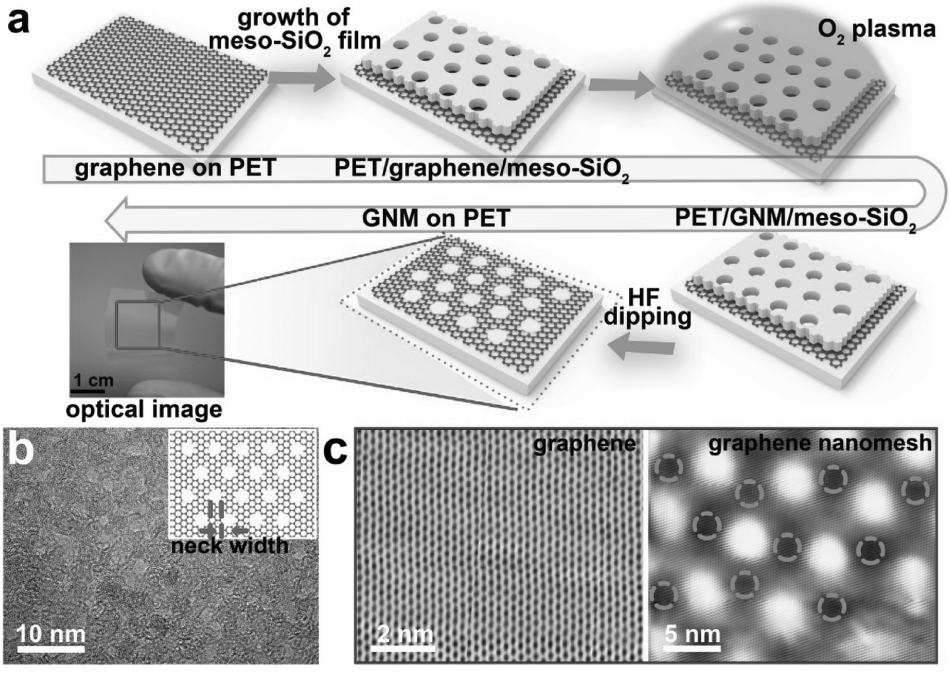

Figure 1. a) Illustration of the fabrication process of GNM. b) TEM image of GNM. Insets of (b): Structural model of GNM. c) STM images of the pristine graphene and GNM, respectively. The dashed circles highlight pores present in the GNM.

areas with different heights arranged in a nearly close-packed structure similar to the meso-SiO_2 pattern and the neck width is about 3 nm. The hexagonally arranged pores can be distinguished from the dark contrast regions that are highlighted by the dashed blue circles. This observation further confirmed the periodic patterned porous structure of the GNM sheet.

As shown in **Figure 2**a, the D and G bands in the Raman spectra of the graphene correspond to the disordered structure and C—C sp^2 bonding (E_{2g}) in graphitic sheets.[44] The intensity of I_D/I_G and I_{2D}/I_G illustrates the defect degree and layer numbers of graphene, respectively.[44] For the pristine graphene, the I_{2D}/I_G has a high value of 4.3 and there is no D peak observed in the curve, indicating the high quality of graphene with single-layer structure. As the O_2 plasma etching proceeds, the D peak gradually appears, revealing the formation of sp^3 defects. A prominent D band arises when the O_2 plasma etching time is 30 s or even longer, indicating the presence of a large number of oxidized graphene edges.[44] In addition, the double-resonance 2D peak is strongly weakened. The

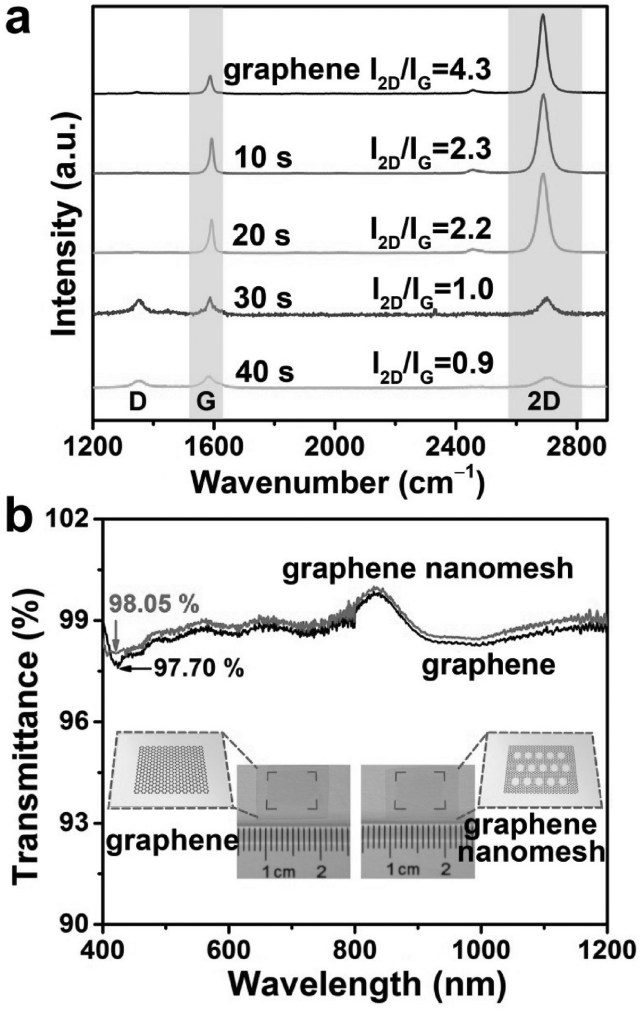

Figure 2. a) Raman spectra of the pristine graphene and GNM obtained for different O_2 plasma etching times. b) UV–vis–NIR spectra of the pristine graphene and GNM. Insets: Optical images and structural models of the pristine graphene and GNM.

decreased sp^2-hybridized carbon and increased C—O and C=O, as shown in the high-resolution X-ray photoelectron spectra (XPS) (Figure S5, Supporting Information), demonstrate the increased oxygen defects in the GNM. The Raman and XPS observations suggest the presence of a large number of oxygen defects, which originate from the O_2 plasma etching process. The UV–vis–NIR spectra indicate that the GNM has a transmittance of 98.05% (Figure 2b), which is slightly higher than that of pristine single-layer graphene with a 97.7% transmittance. The optical images in the inset of Figure 2b illustrate that the GNM retains the structure integrity of the pristine graphene. The resulting GNM with high optical transmittance and structural integrity is very suitable for use in flexible and transparent electronic devices.

Field-effect responses of the GNM were characterized after patterning the material with identical dimensions on the flexible PET substrate (**Figure 3**a, Figure S6, Supporting Information). Figure 3b shows the transfer characteristic of a typical GNM transistor with the neck width of 3.7 nm. The obtained current on/off ratio is 842 at $V_d = -0.01$ V, significantly higher than the on/off ratio of 2 obtained in the pristine graphene (Figure S7, Supporting Information), confirming that the GNM exhibits enhanced semiconducting properties. The output characteristic recorded from the same device suggests that carrier transport is effectively controlled by the top-gate bias (Figure 3c). Importantly, the current on/off ratio as well as the bandgap of the GNM could be readily tuned by changing the plasma etching time during the fabrication process. The GNM prepared by 10 s O_2 plasma etching time results in a neck width of 7 nm, and the resulting current on/off ratio is about 50 (Figure 3d, Figures S8 and S9, Supporting Information). The on/off ratio significantly increases to 3×10^3 for the GNM with neck width of 2.7 nm obtained by an etching time of 40 s. In the case of graphene nanoribbon, the on/off ratio and bandgap are inversely proportional to the nanoribbon width.[38–41] Here, the observed improved on/off ratio with decreasing neck width is consistent with the characteristics of graphene nanoribbons. The semilog of the on/off ratio value versus the inverse of the neck width of GNM is plotted in Figure 3d. The I_{on}/I_{off} ratio can be fit by Equation S1 (Supporting Information) (solid line in Figure 3d). The corresponding bandgap values of GNM can reach to 245 meV (inset of Figure 3d; Equation S2, Supporting Information). The above electronic characteristics suggest that the formation of GNM can effectively enable a semiconducting atomic thin film. Importantly, the fabrication process shows great versatility in controlling the pore wall width and eventually tuning the on/off ratio of GNM. The availability of such GNM in the deep nanometer regime is of vital importance for achieving room temperature FET manipulation and will enable promising opportunities in highly sensitive biosensors.

Figure 4a shows a schematic illustration of the large area GNM FET arrays on the flexible PET substrate. Here, the flexible characteristics of the GNM transistors were investigated by bending the supporting PET substrate to different angles (Figure 4b). The on/off ratio shows a slightly decrease as the bending angles are increased from 30° to 120° (corresponding to the bending radius of 15.2, 7.6, 5.1, and 3.8 mm, respectively), suggesting that the GNM-based FETs exhibit excellent bending endurance throughout the entire bending process. The

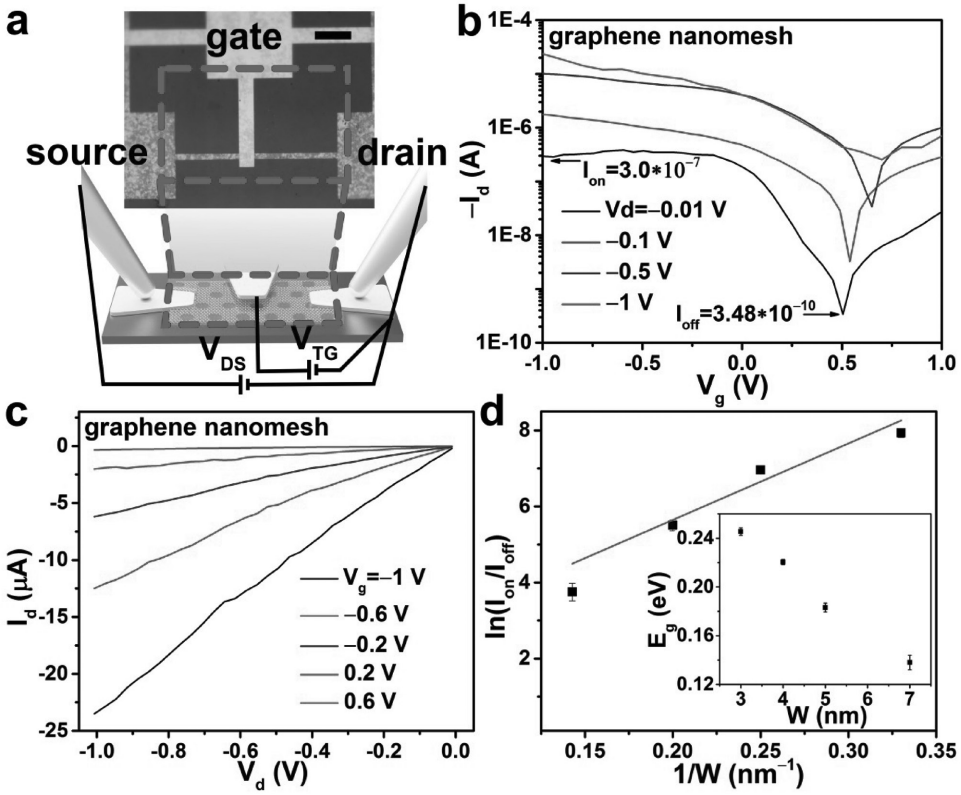

Figure 3. a) Schematic and optical microscopy image of a typical GNM FET device. Scale bar is 5 μm. b) Transfer characteristics for the GNM device recorded at different source-drain voltages (V_d) with channel length and width of 2 μm. c) Drain current (I_d) versus V_d curves for device in panel (b) at different gate voltages (V_g). d) Semilog plot of measured I_{on}/I_{off} as a function of the inverse of the neck width ($1/w$) of GNM. Inset of (d): Energy bandgap (E_g) versus the neck width (w) of GNM. The error bars present the standard deviations of three measurements.

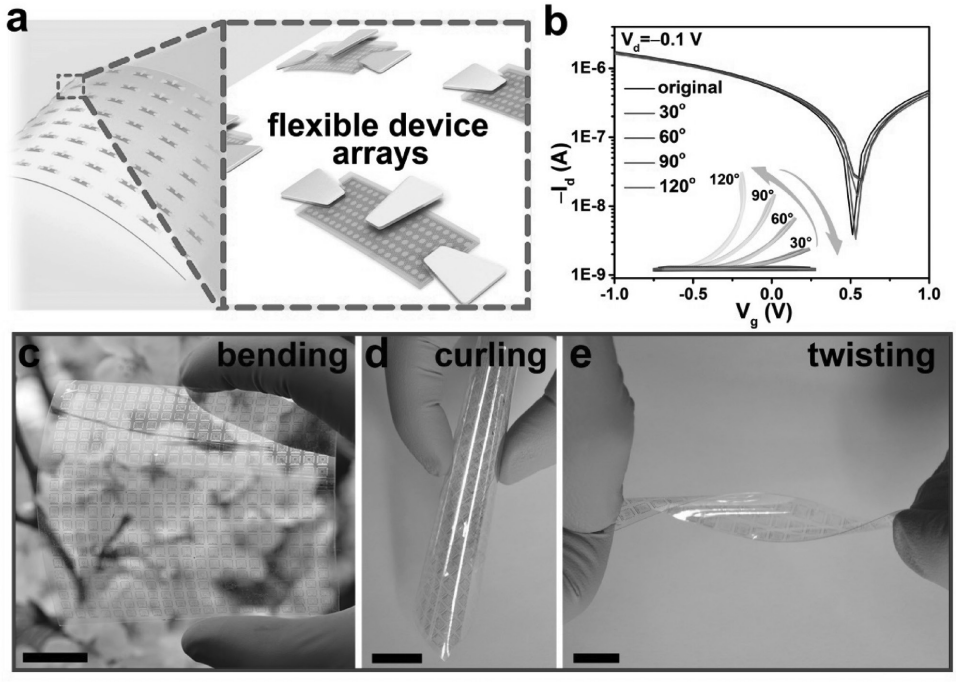

Figure 4. a) Structural models of GNM FET device arrays on flexible PET substrate. b) I_d as a function of V_g at bending angle of 30°, 60°, 90°, and 120°, respectively. The V_d is fixed at –0.1 V. Optical images of the transparent and flexible GNM FET device arrays under c) bending, d) curling, and e) twisting conditions, respectively. Scale bars are 2 cm.

decreased on/off ratio can be associated with the cracks formation in the gate dielectric layer[12] and the enlarged neck width of GNM under the large deformation.[45] The optical images in Figure 4c–e show the flexible and transparent device arrays under bending, curling, and twisting conditions, respectively. The superior flexibility and excellent electronic performance of GNM device make them well suited for wearable, large area electronics and biosensors.

The GNM FET with high on/off ratio as well as large surface-to-volume ratio can be used to construct highly sensitive biosensors since a small variation in the local charges will lead to a significant conductance change. Additionally, the rich edge sites around the pores facilitate the functionalization of specific receptors for the creation of highly specific biosensors that only respond to a certain targeting ligands.[21,46] Also, the pores present in the GNMs can reduce the density of receptor molecules and decrease the steric hindrance when the receptor molecules were interacted with targeting ligands.[47] To this end, we have functionalized the GNM with HER2-specific aptamer for the highly specific detection of HER2, a transmembrane protein that is overexpressed by 100-fold or more on the surface of breast cancer cells.[16,48] **Figure 5**a shows the schematic illustration of the aptamer modification and subsequent protein binding process. The 1-pyrenebutanoic acid succinimidyl ester linker conjugated with the amino modified HER2-specific aptamer through the formation of an amide bond. Figure 5b shows the designed transparent, flexible integrated device intimately attached onto the human skin, demonstrating the superior mechanical flexibility of the polydimethylsiloxane (PDMS) substrate and its integrated GNM electronic components. The device can be bended and released continuously by the folding and unfolding motion of the wrist (Figure S15, Supporting

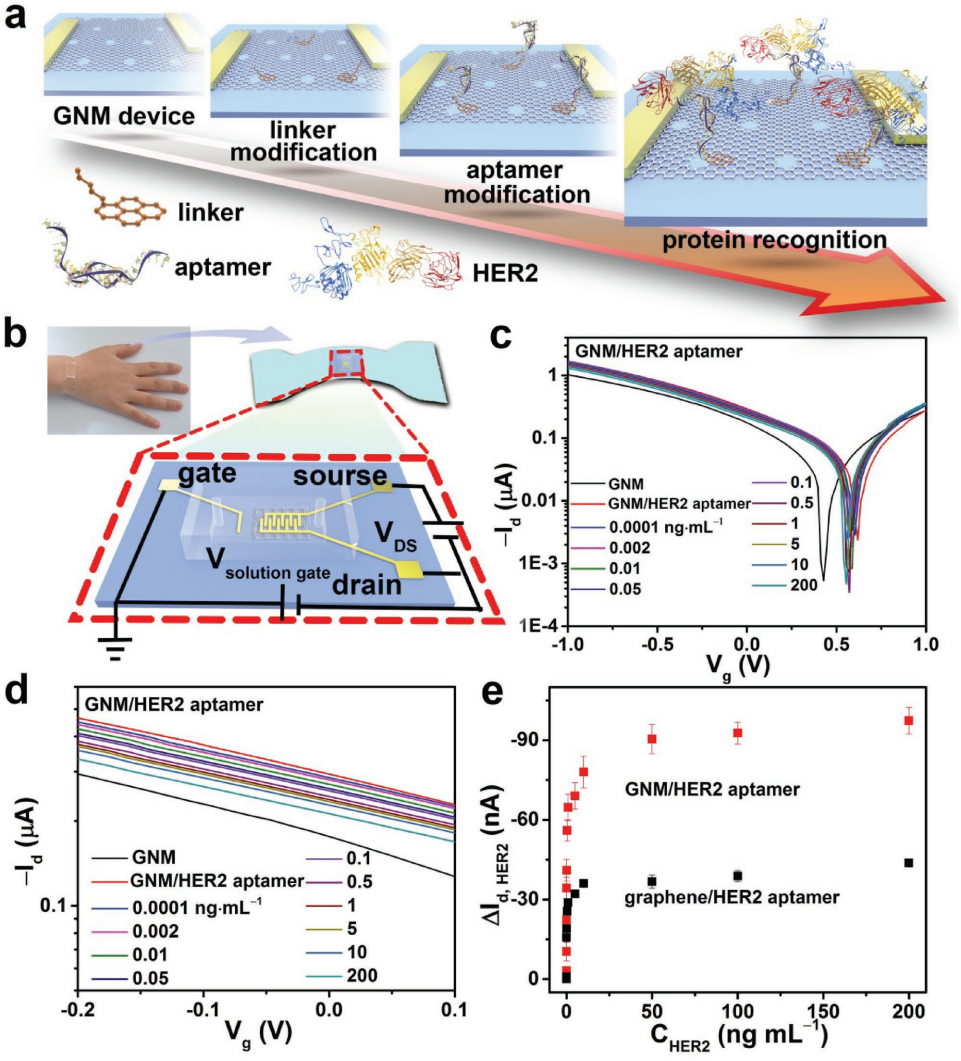

Figure 5. GNM FET biosensor. a) Schematic illustration of the fabrication of GNM FET biosensor. b) GNM FET biosensor integrated on the PDMS film and attached on the human skin. Enlarged views: Corresponding schematic structure of the flexible biosensor. c) Transfer characteristics of solution-gated GNM FET biosensor in response to HER2 protein concentrations ranging from 0.0001 to 200 ng mL^{-1}. The V_d is set at a fixed value of –0.1 V. d) Magnified curve of (c) in the V_g range of –0.2–0.1 V. e) Current change ($\Delta I_{d,\ HER2}$) versus HER2 concentration (C_{HER2}). The error bars present the standard deviations of three measurements.

Information), demonstrating that the designed flexible biosensor holds great promise to serve as implantable electronics.

The aptamer-modified GNM sensors are operated by measuring the drain current versus gate voltage when subjected to HER2 solutions (Figure 5c,d). The HER2 proteins interact with the aptamers attached on the GNM surface, which in turn induce the electrical signal change in the GNM-based biosensor.[17,49] The interactions between the aptamer and HER2 protein can affect the charge-carrier density on the surface of the GNMs and allow label-free detection using the FET biosensor. As shown in Figure 5c,d, the drain current has a significant increase (120 nA) after the immobilization of negatively charged HER2 aptamer, indicating that the modification of aptamers induces the accumulation of negative charge carriers in the GNM channel. Since the carriers in the GNM channel are holes,[38,49] this increased current indicates that the negatively charged HER2 aptamer acts as a negative gate to increase hole density. The aptamer functionalized GNM device exhibits a current decrease of 3 nA upon recognizing the HER2 with a concentration of 0.0001 ng mL^{-1} and then shows a consistent decrease in current as the HER2 concentration increases from 0.0001 to 200 ng mL^{-1}. This observed decrease in channel current can be explained by the decrease of hole charge density in p-type GNM upon the binding of positively charged HER2[16] onto the negatively charged aptamer. Specifically, the positively charged HER2 molecules can effectively screen the negative charges in the aptamer. The increased binding of HER2 protein molecules induces the gradually decrease of negatively charged carriers on the aptamer conjugated GNMs and thus the current of the GNM biosensor. Therefore, the binding of positively charged HER2 to aptamer is equivalent to positive gating aptamer functionalized GNM, which reduces hole density and the current. The leakage current through the solution gate (<0.4 nA) (Figure S18, Supporting Information) is negligible compared with the source-drain current of the GNM biosensors (≈1 µA). Figure 5e plots the relationship between the drain current ($\Delta I_{d,\ HER2}$) and the HER2 concentration (C_{HER2}). It is shown that $\Delta I_{d,\ HER2}$ exhibits a sharply increase as the C_{HER2} increases from 0.0001 to 10 ng mL^{-1} and then gradually becomes saturated above 10 ng mL^{-1}. The specific binding between aptamer and HER2 in the GNM channel follows the Langmuir adsorption isotherm (Equation S3, Supporting Information). From the fitted curve of $C_{HER2}/\Delta I_{d,\ HER2}$ versus C_{HER2} (Figure S19, Supporting Information), the calculated dissociation constant (K_d) of the aptamer-HER2 complex is estimated to be 13×10^{-12} M, indicating a high affinity between the HER2 aptamer and HER2 protein. The sensitivity change (S) gradually increased linearly up to a HER2 concentration of 10 ng mL^{-1} (Figure S19, Supporting Information). The linear working range of the GNM-FET biosensor for HER2 protein detection is in the range of 0.0001 to 10 ng mL^{-1} (Figure S19, Supporting Information).

Control experiments (with nonspecific proteins) verified that our designed GNM exhibits high specificity and selectivity due to aptamer immobilization (Figure S20, Supporting Information). The real-time electrical responses of GNM device to HER2 indicating that the time dependent $\Delta I_{d,\ HER2}$ exhibits a stepwise current increase upon the binding of HER2 with increasing concentration (**Figure 6**a). The HER2 protein

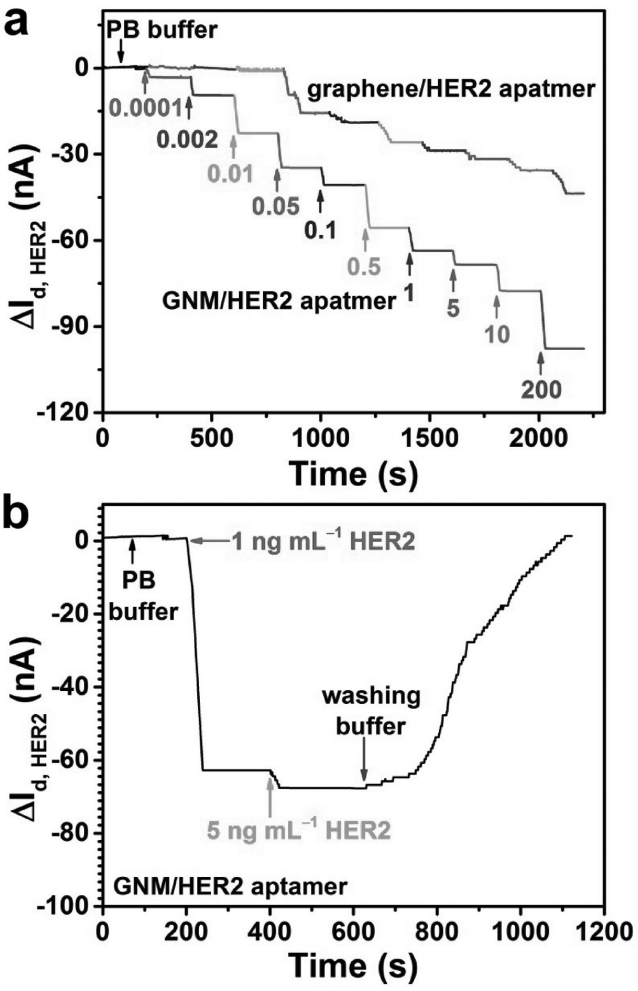

Figure 6. a) Real-time electrical measurement of different concentrations of HER2 based on the GNM and graphene, respectively. b) Real-time sensor response to the successive injection of different concentrations of HER2 and subsequent PB buffer washing.

solution with a concentration of 0.1 pg mL^{-1} causes a significant current change of 3 nA. The lowest detection limit of the GNM biosensor is observed to be as low as 0.6×10^{-15} M (corresponding to a concentration of 0.1 pg mL^{-1}), significantly lower than the pristine graphene-based biosensor (Figure 6a). In this case, the amount of HER2 molecules absorbed on aptamer conjugated GNM is quantified to be nearly 3600-HER2 molecules. To our best knowledge, this is the lowest detection limit toward HER2 protein on the cancer cell surface.[16,50] In comparison, the device based on the pristine graphene modified with aptamer shows a much lower response of 1 nA even with a large HER2 concentration of 60×10^{-15} M (0.01 ng mL^{-1}) (Figure 6a; Figure S21, Supporting Information). Also, the GNM-based biosensor exhibits a higher sensitivity than that of graphene. The improved sensitivity of the GNM biosensor can be associated with the increased on/off ratio, which reduces the current leakages in an off state and induces a large current change even under a small environmental variation.[17,49] In addition, the large surface area of GNMs optimizes the density of aptamer on the device surface to obtain the maximum

number of protein or cells without causing significant steric repulsion.[21,47] To confirm the enhanced recognition effect, we performed the atomic force microscopy characterizations (Figure S23, Supporting Information). It can be seen that the biosensor device based on GNM was considerably roughened after recognizing the protein molecules. More importantly, the GNM exhibits a higher protein binding amount than that of graphene due to the increased edge sites around the pores and enlarged surface area. Furthermore, the functionalized GNM device exhibits rapid response speed (Figure 6a). The average response time of GNM biosensor is less than 10 s, which is limited by the diffusion at the interface of different HER2 concentrations.[13] Figure 6b shows the real time current trace recorded during the addition of phosphate-buffer (PB), then the incorporation of HER2 solution, and finally rinsing with PB. The current level exhibits a fast decrease and then gradually recovers to the original level, demonstrating the fast recovery and excellent reusability of the GNM device. The sensing measurements clearly demonstrate that the fabricated GNM-based device with high on/off ratio can be used as highly sensitive biosensors for the detection of cancer biomarkers. In this well-designed nanodevice system, the specific aptamer enables the highly selective recognition of HER2, and meanwhile, the large surface area facilitates efficient analyte binding and at the same time offers easy patternability and device fabrication. Additionally, the excellent flexibility of the integrated devices promises its application to high-performance wearable biosensor.

A further in vitro test with the aptamer-functionalized biosensors for real-time probing HER2 protein on the surface of SK-BR-3 cell was performed. **Figure 7**a shows the corresponding optical microscope image of the SK-BR-3 cells seeded on the aptamer-modified GNM device, indicating that the cells are conformally attached to the FET device surface. The specific binding of the device with SK-BR-3 cells is realized by the specific recognition of HER2 protein on the cell surface (Figure 7b). Figure 7c shows the representative time-dependent response of the sensor upon the addition of SK-BR-3 cells. The confocal fluorescence microscopy images of the fluorescent-labeled SK-BR-3 cells were also collected to investigate the gradually recognition and binding of cells to the GNM device. According to Figure 7c, a 0.2 nA current reduction is observed upon the binding of a single cell, and the current exhibits a significant and continuous decrease with the increase of cells binding on the device surface. The decreased current is attributed to the binding of aptamer to positively charged HER2 protein on the cell surface. The current variation of the control sample remained as the same value during the measurement. It is worth mentioning that the current variation upon the recognition of cells is lower than that of protein molecules. The reasons lie in that the 2D planar device can only recognize the cells partly.[51,52] Additionally, the random distribution of protein molecules on the cell surface is an important factor that influences the aptamer-cell interaction.[48] The measurements for nonspecific CEM cells show a negligible current change (Figure S25, Supporting Information), suggesting that the HER2 aptamer exhibits low binding affinity to nonspecific cells and a high specific recognition ability to target cells. The above results thus demonstrated that the aptamer-functionalized GNM biosensor can be used for highly sensitive and selective detection of cancer cells with a detection limit of a single cell. This superior performance is attributed to the high-spatial resolution and relative low operation potential of our fabricated GNM-based biosensor. The extremely high sensitivity in combination with the intrinsic flexibility of the GNM device demonstrates the exceptional promise for practical applications in complex biological systems for early disease diagnosis.

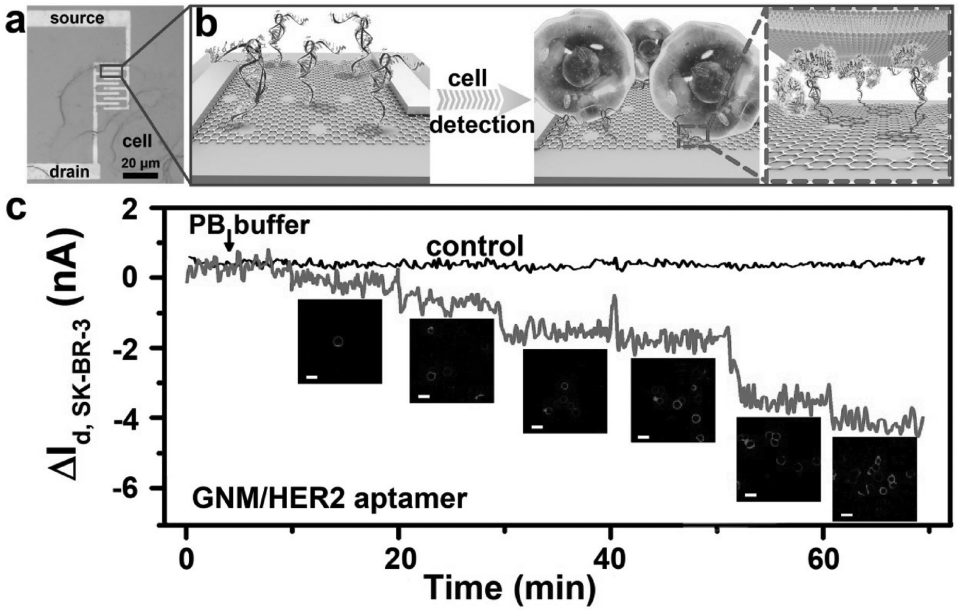

Figure 7. a) Optical microscope image of SK-BR-3 cells seeded on the GNM FET biosensor. b) Schematic illustration of the biosensor's selective recognition of SK-BR-3 cells. c) Real-time biosensor measurement of the binding of cells to the device surface. Insets: Corresponding fluorescence images of fluorescent-labeled SK-BR-3 cells. Scale bars are 40 μm.

3. Conclusion

To summarize, a rationally designed GNM-based flexible FET biosensor was demonstrated for the first time. The GNMs with variable neck widths down to 2.7 nm have been prepared using a large-area meso-SiO_2 film as etch mask. The FET device prepared by using GNM as the semiconducting channel material exhibits high room temperature on/off ratio and neck width-dependent bandgap. Importantly, the on/off ratio exceeds 3 orders of magnitude when the neck width is reduced to 2.7 nm. The high on/off ratio of the GNM-based device enables high sensitivity and rich edge sites and large surface-to-volume ratio benefits for target analyte attachment. After modification with HER2-specific aptamer, the GNM biosensors can allow highly sensitive and selective detection of HER2 protein with detection limit down to 0.6×10^{-15} M. In addition, the fabricated device can serve as a label-free biosensor for in vitro detection of SK-BK-3 cells at the single-cell level. The development of such GNM provides a promising strategy for developing high-performance, flexible, and label-free biosensors for next-generation low cost clinical disease diagnosis.

Supporting Information

Supporting Information is available from the Wiley Online Library or from the author.

Acknowledgements

This work was supported by the National Natural Science Foundation of China (Grant Nos. 21422105 and 51325202) and the Ten Thousand Talents Program for Young Talents. The authors would like to acknowledge the support from Prof. Y. Fang (National Center for Nanoscience and Technology, Beijing, China) for the help of the synthesis of low-pressure CVD graphene. Q.Y. thanks for Prof. Z. F. Liu (Peking University) and his group for technical support regarding STM characterizations.

Received: August 10, 2016
Revised: October 7, 2016
Published online:

[1] W. Gao, S. Emaminejad, H. Y. Y. Nyein, S. Challa, K. Chen, A. Peck, H. M. Fahad, H. Ota, H. Shiraki, D. Kiriya, D.-H. Lien, G. A. Brooks, R. W. Davis, A. Javey, *Nature* **2016**, *529*, 509.
[2] D. Son, J. Lee, S. T. Qiao, R. Ghaffari, J. Kim, J. E. Lee, C. Song, S. J. Kim, D. J. Lee, S. W. Jun, S. X. Yang, M. Park, J. Shin, K. Do, M. Lee, K. Kang, C. S. Hwang, N. S. Lu, T. Hyeon, D.-H. Kim, *Nat. Nanotechnol.* **2014**, *9*, 397.
[3] T. Q. Trung, N.-E. Lee, *Adv. Mater.* **2016**, *28*, 4338.
[4] T. D. Nguyen, N. Deshmukh, J. M. Nagarah, T. Kramer, P. K. Purohit, M. J. Berry, M. C. McAlpine, *Nat. Nanotechnol.* **2012**, *7*, 587.
[5] Z. T. Li, Z. L. Wang, *Adv. Mater.* **2011**, *23*, 84.
[6] B. Z. Tian, T. Cohen-Karni, Q. Qing, X. J. Duan, P. Xie, C. M. Lieber, *Science* **2010**, *329*, 830.
[7] S. Yun, S. Park, B. Park, Y. Kim, S. K. Park, S. Nam, K.-U. Kyung, *Adv. Mater.* **2014**, *26*, 4474.
[8] X. L. Xu, B. Peng, D. H. Li, J. Zhang, L. M. Wong, Q. Zhang, S. J. Wang, Q. H. Xiong, *Nano Lett.* **2011**, *11*, 3232.
[9] L. F. Wang, B. Wu, J. S. Chen, H. T. Liu, P. A. Hu, Y. Q. Liu, *Adv. Mater.* **2014**, *26*, 1559.
[10] L. Liao, J. W. Bai, Y.-C. Lin, Y. Q. Qu, Y. Huang, X. F. Duan, *Adv. Mater.* **2010**, *22*, 1941.
[11] W. H. Lee, J. Park, S. H. Sim, S. B. Jo, K. S. Kim, B. H. Hong, K. Cho, *Adv. Mater.* **2011**, *23*, 1752.
[12] S.-K. Lee, H. Y. Jang, S. Jang, E. Choi, B. H. Hong, J. Lee, S. Park, J.-H. Ahn, *Nano Lett.* **2012**, *12*, 3472.
[13] S. Jiang, R. Cheng, X. Wang, T. Xue, Y. Liu, A. Nel, Y. Huang, X. F. Duan, *Nat. Commun.* **2013**, *4*, 2225.
[14] R. Stine, J. T. Robinson, P. E. Sheehan, C. R. Tamanaha, *Adv. Mater.* **2010**, *20*, 5297.
[15] Y. Ohno, K. Maehashi, K. Matsumoto, *J. Am. Chem. Soc.* **2010**, *132*, 18012.
[16] S. Myung, A. Solanki, C. Kim, J. Park, K. S. Kim, K.-B. Lee, *Adv. Mater.* **2011**, *23*, 2221.
[17] O. S. Kwon, S. J. Park, J.-Y. Hong, A. R. Han, J. S. Lee, J. S. Lee, J. H. Oh, J. Jang, *ACS Nano* **2012**, *6*, 1486.
[18] M. Zhang, C. Z. Liao, C. H. Mak, P. You, C. L. Mak, F. Yan, *Sci. Rep.* **2015**, *5*, 8311.
[19] D. Sarkar, W. Liu, X. J. Xie, A. C. Anselmo, S. Mitragotri, K. Banerjee, *ACS Nano* **2014**, *8*, 3992.
[20] a) M. Larisika, C. Kotlowski, C. Steininger, R. Mastrogiacomo, P. Pelosi, S. Schütz, S. F. Peteu, C. Kleber, C. Reiner-Rozman, C. Nowak, W. Knoll, *Angew. Chem., Int. Ed.* **2015**, *54*, 13245; b) M. Larisika, C. Kotlowski, C. Steininger, R. Mastrogiacomo, P. Pelosi, S. Schütz, S. F. Peteu, C. Kleber, C. Reiner-Rozman, C. Nowak, W. Knoll, *Angew. Chem.* **2015**, *127*, 13443.
[21] B. Zribi, J.-M. Castro-Arias, D. Decanini, N. Gogneau, D. Dragoe, A. Cattoni, A. Ouerghi, H. Korri-Youssoufi, A.-M. Haghiri-Gosnet, *Nanoscale* **2016**, *8*, 15479.
[22] P. Avouris, *Nano Lett.* **2010**, *10*, 4285.
[23] F. Schwierz, *Nat. Nanotechnol.* **2010**, *5*, 487.
[24] Z. Li, Z. Liu, H. Y. Sun, C. Gao, *Chem. Rev.* **2015**, *115*, 7046.
[25] C. X. Chen, J. Z. Wu, K. T. Lam, G. S. Hong, M. Gong, B. Zhang, Y. Lu, A. L. Antaris, S. Diao, J. Guo, H. J. Dai, *Adv. Mater.* **2015**, *27*, 303.
[26] B. G. Choi, H. Park, T. J. Park, M. H. Yang, J. S. Kim, S.-Y. Jang, N. S. Heo, S. Y. Lee, J. Kong, W. H. Hong, *ACS Nano* **2010**, *4*, 2910.
[27] O. S. Kwon, S. H. Lee, S. J. Park, J. H. An, H. S. Song, T. Kim, J. H. Oh, J. Bae, H. Yoon, T. H. Park, J. Jang, *Adv. Mater.* **2013**, *25*, 4177.
[28] M. Kim, N. S. Safron, E. Han, M. S. Arnold, P. Gopalan, *Nano Lett.* **2010**, *10*, 1125.
[29] L. Liu, Y. L. Zhang, W. L. Wang, C. Z. Gu, X. D. Bai, E. Wang, *Adv. Mater.* **2011**, *23*, 1246.
[30] J. W. Bai, X. F. Duan, Y. Huang, *Nano Lett.* **2009**, *9*, 2083.
[31] X. G. Liang, Y.-S. Jung, S. W. Wu, A. Ismach, D. L. Olynick, S. Cabrini, J. Bokor, *Nano Lett.* **2010**, *10*, 2454.
[32] X. L. Li, X. R. Wang, L. Zhang, S. Lee, H. J. Dai, *Science* **2008**, *319*, 1229.
[33] L. Talirz, P. Ruffieux, R. Fasel, *Adv. Mater.* **2016**, *28*, 6222.
[34] L. Liao, Q. Xie, X. F. Guo, Z. F. Liu, *Adv. Mater.* **2015**, *27*, 4093.
[35] S. Y. Lee, D. L. Duong, Q. A. Vu, Y. Jin, P. Kim, Y. H. Lee, *ACS Nano* **2015**, *9*, 9034.
[36] D. V. Kosynkin, A. L. Higginbotham, A. Sinitskii, J. R. Lomeda, A. Dimiev, B. K. Price, J. M. Tour, *Nature* **2009**, *458*, 872.
[37] L. M. Xie, L. Y. Jiao, H. J. Dai, *J. Am. Chem. Soc.* **2010**, *132*, 14751.
[38] J. W. Bai, X. Zhong, S. Jiang, Y. Huang, X. F. Duan, *Nat. Nanotechnol.* **2010**, *5*, 190.
[39] J. W. Bai, X. F. Duan, Y. Huang, *Nano Lett.* **2009**, *9*, 2083.
[40] W. J. Yu, X. F. Duan, *Sci. Rep.* **2013**, *3*, 1248.
[41] W. J. Yu, L. Liao, S. H. Chae, Y. H. Lee, X. F. Duan, *Nano Lett.* **2011**, *11*, 4759.
[42] Z. Y. Zeng, X. Huang, Z. Y. Yin, H. Li, Y. Chen, H. Li, Q. Zhang, J. Ma, F. Boey, H. Zhang, *Adv. Mater.* **2012**, *24*, 4138.

[43] a) Z. G. Teng, G. F. Zheng, Y. Q. Dou, W. Li, C.-Y. Mou, X. H. Zhang, A. M. Asiri, D. Y. Zhao, *Angew. Chem., Int. Ed.* **2012**, *51*, 2173; b) Z. G. Teng, G. F. Zheng, Y. Q. Dou, W. Li, C.-Y. Mou, X. H. Zhang, A. M. Asiri, D. Y. Zhao, *Angew. Chem.* **2012**, *124*, 2215.
[44] L. Zhou, L. Liao, J. Y. Wang, J. W. Yu, D. H. Li, Q. Xie, Z. R. Liu, Y. L. Yang, X. F. Guo, Z. F. Liu, *Adv. Mater.* **2016**, *28*, 2148.
[45] Q. Y. He, S. X. Wu, S. Gao, X. H. Cao, Z. Y. Yin, H. Li, P. Chen, H. Zhang, *ACS Nano* **2011**, *5*, 5038.
[46] Y. N. Chen, Z. P. Michael, G. P. Kotchey, Y. Zhao, A. Star, *ACS Appl. Mater. Interfaces* **2014**, *6*, 3805.
[47] S. S. Mahshid, S. Camiré, F. Ricci, A. Vallée-Bélisle, *J. Am. Chem. Soc.* **2015**, *137*, 15596.
[48] H. Lee, D. H. M. Dam, J. W. Ha, J. Yue, T. W. Odom, *ACS Nano* **2015**, *9*, 9859.
[49] S. J. Park, O. S. Kwon, S. H. Lee, H. S. Song, T. H. Park, J. Jang, *Nano Lett.* **2012**, *12*, 5082.
[50] Y. Zhu, P. Chandra, Y.-B. Shim, *Anal. Chem.* **2013**, *85*, 1058.
[51] H.-M. So, D.-W. Park, E.-K. Jeon, Y.-H. Kim, B. S. Kim, C.-K. Lee, S. Y. Choi, S. C. Kim, H. Chang, J.-O. Lee, *Small* **2008**, *4*, 197.
[52] M. S. Mannoor, H. Tao, J. D. Clayton, A. Sengupta, D. L. Kaplan, R. R. Naik, N. Verma, F. G. Omenetto, M. C. McAlpine, *Nat. Commun.* **2012**, *3*, 763.